International Journal of Solids and Structures 46 (2009) 3027–3044

Contents lists available at ScienceDirect

International Journal of Solids and Structures

journal homepage: www.elsevier.com/locate/ijsolstr

Evolution of plasticity in notched Ni-base superalloy single crystals

N.K. Arakere [a,*], S. Siddiqui [a], F. Ebrahimi [b]

[a] Mechanical and Aerospace Engineering, 237 MAE-B Building, University of Florida, Gainesville, FL 32611-6300, USA
[b] Materials Science and Engineering, University of Florida, USA

ARTICLE INFO

Article history:
Received 22 June 2008
Received in revised form 6 April 2009
Available online 14 April 2009

Keywords:
Single crystal
Superalloy
Tensile testing
Notch tip plasticity
Anisotropic material
Crystal plasticity
Finite element analysis

ABSTRACT

Numerical and experimental investigations of evolution of slip fields in notched Ni-base superalloy single crystal tensile specimens are presented as functions of load and secondary (notch) orientation. Three crystallographic orientations were investigated with the primary (load) orientation fixed along the [001] direction while the notch directions are parallel to $[\bar{1}10]/[1\bar{1}0]$, $[010]/[0\bar{1}0]$, and $[\bar{3}10]/[3\bar{1}0]$, respectively. A three-dimensional elastic *anisotropic* finite element analysis (FEA) was used to compute the triaxial stress fields in the neighborhood of the notch. The elastic solution is successful in identifying which slip systems are activated initially. Interestingly this procedure was found to be also successful in predicting slip evolution at higher loads, because of slip localization in the superalloy tested. Based on this analysis, the concept of "dominant slip system" is introduced and defined as the single slip system that experiences the highest resolved shear stress (RSS) at a given point near the notch. The dominant slip systems are seen to persist with increasing load and inhibit the activation of new slip systems, which implies that when plasticity is initiated in the dominant slip systems, either softening takes place and/or the rate of increase in RSS on the other slip systems is reduced significantly. The distribution of dominant slip systems in the neighborhood of the notch and on the surface is used to accurately predict the evolution of activated slip sectors and sector boundaries observed experimentally. The activated stress fields are shown to vary strongly through the specimen thickness. Elastic anisotropy governs the development of the elastic stress field and controls which slip systems become initially dominant/activated. Therefore inclusion of elastic anisotropy was found to be important for the prediction of stress field evolution as functions of load and crystal orientation.

1. Introduction

Single crystals are both elastically and plastically anisotropic and their properties depend on crystallographic orientation. In metallic single crystals, plasticity precedes fracture, and fracture is influenced both by elastic and plastic anisotropy in the neighborhood of the crack tip. A large number of studies have focused on the effect of crystallographic orientation on plastic deformation of smooth specimens; however, only limited work has been reported on the development of plastic zones at meso- and macroscopic levels in notched ductile single crystals. Towards addressing this gap we present an experimental and numerical investigation of evolution of slip (plasticity) fields in triaxial stress fields induced in notched single crystal tensile specimens as a function of load and secondary (notch) orientation.

Single crystal superalloy turbine blades and vanes, used in aircraft and rocket engines, are subject to high operating temperatures, corrosive environments, and high monotonic and cyclic stresses. The major cause of the blade failure is the nucleation and propagation of fatigue cracks from regions of high stress concentration such as notches. There is as yet no generally accepted quantitative description of the fatigue crack nucleation process in a single crystal. The factors that play an important role in fatigue crack nucleation are thought to be the magnitudes of resolved shear stress (RSS) on the slip planes and the normal stress on the slip plane with the highest resolved shear stress (Nalla et al., 2002). Dunne et al. (2007) have shown that crack nucleation occurs at free surface locations where slip banding was predicted by crystal plasticity simulations and highlights the important role of persistent slip bands (PSBs) and accumulated slip in fatigue crack nucleation. Additionally, crystallographic fatigue cracks have been shown to nucleate and propagate on {111} slip planes in single crystal superalloys (Deluca and Annis, 1995). To identify crack nucleation mechanisms, it is therefore important to understand how plasticity evolves and becomes localized in notches or regions of stress concentration.

Rice (1987) presented an asymptotic analysis of the plane strain field at a crack tip in an elastic-ideally plastic crystal, for two orientations ([010] load and $([10\bar{1}]/[\bar{1}0\bar{1}])$ notch directions, [101] load and $[010]/[10\bar{1}]$ notch directions), and predicted a stress field with strong strain localization along certain radial directions

* Corresponding author. Tel.: +1 352 392 0856; fax: +1 352 392 1071.
E-mail address: nagaraj@ufl.edu (N.K. Arakere).

0020-7683/$ - see front matter © 2009 Elsevier Ltd. All rights reserved.
doi:10.1016/j.ijsolstr.2009.04.006

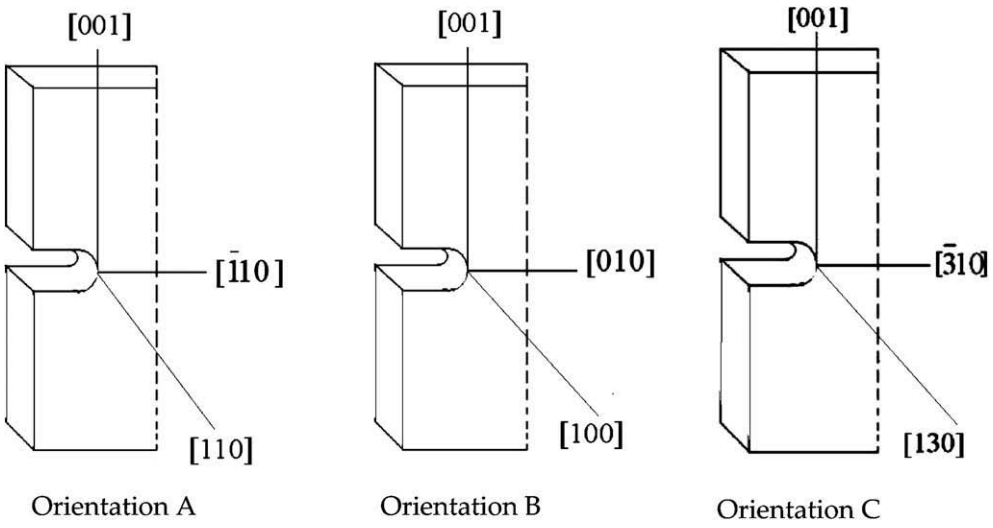

Fig. 1. The three crystallographic orientations investigated in this study.

around the crack tip. Furthermore, the analysis showed that the stress remains constant within each sector, and changes discontinuously from sector to sector. Rice's 2D solution yields the same sector boundaries for both orientations studied and also does not distinguish between FCC and BCC crystal structures. Rice acknowledges the simplification of the plane strain assumption and the importance of incorporating anisotropy, strain hardening and three-dimensional (3D) effects into future models. On the footsteps of Rice, Drugan (2001) also derived the asymptotic solutions for the near-tip stress fields for stationary plane strain tensile cracks in elastic-ideally plastic single crystals for both FCC and BCC crystals. Rice predicted kink and slip type of sector boundary for a symmetric orientation whereas Drugan predicted only slip type of sector boundary for the symmetric orientation. Also Drugan's solution predicted different sector boundaries for the FCC and BCC cases and the near-tip stress field solutions differed substantially from one orientation to another, highlighting the importance of including anisotropy. Rice and Saeedvafa (1987) and Saeedvafa and Rice (1988) accounted for effects of hardening near a crack tip, assuming that the crystals obeyed Taylor power law hardening. Shield and Kim (1994) compared experimentally measured plastic deformation fields near a notch tip for an iron single crystal (BCC structure) with Rice's (1987) analytical solution. For the single orientation tested a good agreement between the interior deformation, using dislocation etch pitting, and surface strains, using Moiré analysis, was found, indicating that surface measurements accurately reflect the deformations that are occurring in the interior of the specimen and thus a comparison with the plane strain result of Rice (1987) is justified. Later, Shield (1996) presented experimental results for a notched copper FCC single crystal of the same

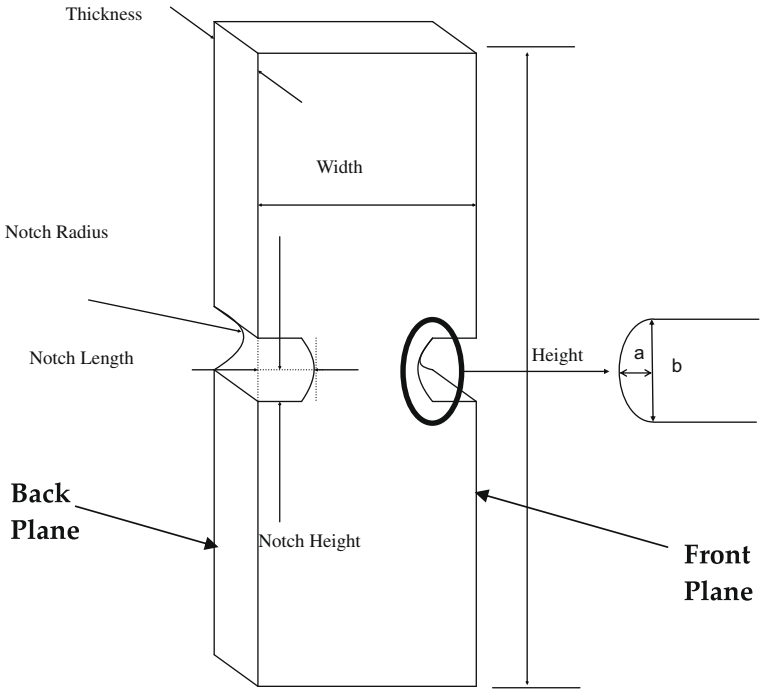

Fig. 2. Specimen geometry of the double-notched tensile specimens (specific dimensions for each orientation are given in Table 1).

orientation as in Shield and Kim (1994) and observed similar slip sector boundaries as in the iron single crystal, but with somewhat different sector boundary angles. Sector boundaries were unaffected by load, even though the notch tip plasticity increases with load. Results obtained for low loads showed similarities to Rice's (1987) model, but not at higher loads with consequently greater plastic strain. Crone and Shield (2001) continued experimental studies of notch tip deformation for two different orientations of single crystal copper and copper–beryllium tensile specimens. Contrary to the equivalent sectors predicted by Rice (1987), Crone and Shield's (2001) observed sectors show a marked difference with orientation, varying in both specific boundary angles and in the number of sectors. Crone et al. (2004) extend their work on slip near copper single crystal notches by examining two symmetric and four nonsymmetric crystallographic orientations to study orientation dependence. Schulson and Xu (1997) examined the state of stress at a notch tip for single crystal Ni_3Al, the γ'-component of single crystal superalloys, using three-point bend specimens. Experimental results were found to deviate from the 2D isotropic solution.

Slip lines are typically observed on the specimen surface and observation through the specimen thickness cannot be seen readily once the specimen is cut. Kysar and Briant (2002) have used electron back-scatter diffraction (EBSD) to observe lattice rotation through the specimen thickness and were able to show the existence of kink bands near the crack tip of aluminum crystals. Flouriot et al. (2003) also use EBSD orientation mapping and 3D FEA to study through-thickness variation of plastic strain fields in a CT single crystal superalloy specimen. Thus there is ample evidence (Cuitino and Ortiz, 1996; Magnan, 2002; Kysar and Briant, 2002; Flouriot et al., 2003; Kim et al., 2003; Arakere et al., 2005; Siddiqui, 2006; Ebrahimi et al., 2006) that the state of stress at a notch is strongly triaxial and changes rapidly from the surface to interior, and that neither plane stress nor plane strain assumptions can adequately describe the surface and midplane stress states, respectively.

We now address certain practical considerations involved in single crystal turbine blade design and their implications for our investigation. The first stage turbine blades made of these very high strength nickel based superalloys used in aircraft propulsion engines and industrial gas turbine (IGT) engines have complex 3D geometry with internal passages for convective cooling and holes at the leading and trailing edges of the turbine airfoil. Directional solidification using grain selectors is used to produce a single crystal with the $\langle 001 \rangle$ low modulus orientation parallel to the growth direction, controlled to within 8–10°. The secondary direction normal to the growth direction, which is typically referenced to a line parallel to the blade attachment, is determined but not controlled. Hence the blade primary orientation is along [001] (radial direction) while the secondary orientation is random, but known, and can vary from 0° to 90°. Fatigue cracks typically nucleate at the blade leading edge cooling hole locations, due to a combination of mechanical and thermal cyclic stresses and strains. There is considerable blade-to-blade variation in the region where fatigue cracks are initiated at the cooling holes because of blade-to-blade secondary orientation variation. Over 95% of blade design in the turbine engine industry is accomplished via 3D elastic anisotropic FEA. Although crystal plasticity analysis is becoming a common tool for research applications, it is still not practical for blade design because of complex 3D geometry and loading involved. Crystal plasticity codes are used mainly for simulating cyclic hysteresis loops and for constitutive

Table 1
Actual and finite element model dimensions of specimen orientations A, B and C in mm.

Dimensions	Orientation A		Orientation B		Orientation C	
	Actual	FEM	Actual	FEM	Actual	FEM
Width	5.100	5.100	5.04	5.04	5.1	5.1
Height	19.00	19.00	17.594	17.594	19.0	19.0
Thickness	1.800	1.800	1.82	1.82	1.77	1.77
Right notch length	1.300	1.550	1.399	1.399	1.4	1.4
Left notch length	1.550	1.550	1.360	1.399	1.39	1.4
Right notch height	0.113	0.113	0.084	0.084	0.085	0.086
Left notch height	0.111	0.113	0.084	0.084	0.086	0.086
a (For both left and right notch)	0.055	0.055	0.056	0.056	0.055	0.055
b (For both left and right notch)	0.226	0.226	0.168	0.168	0.172	0.172

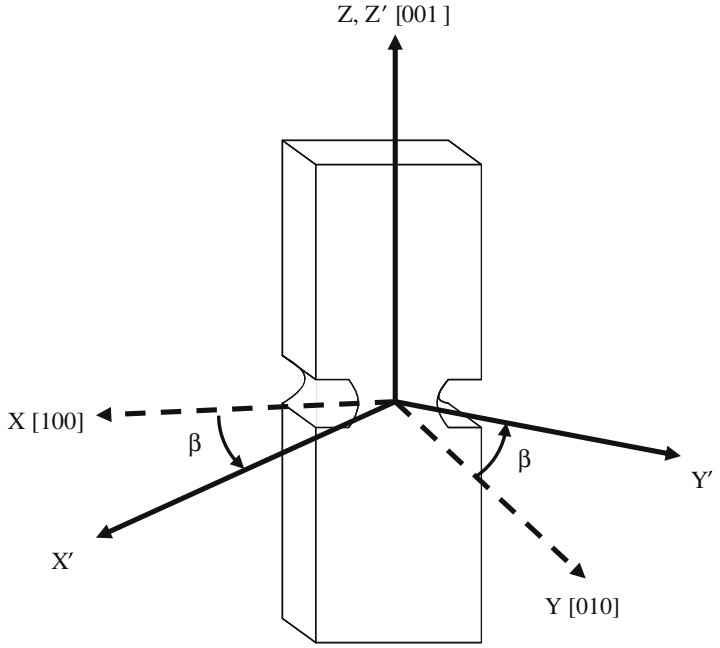

Fig. 3. A schematic defining the material, (X,Y,Z), and specimen, (X',Y',Z'), coordinate systems as well as the secondary orientation, β.

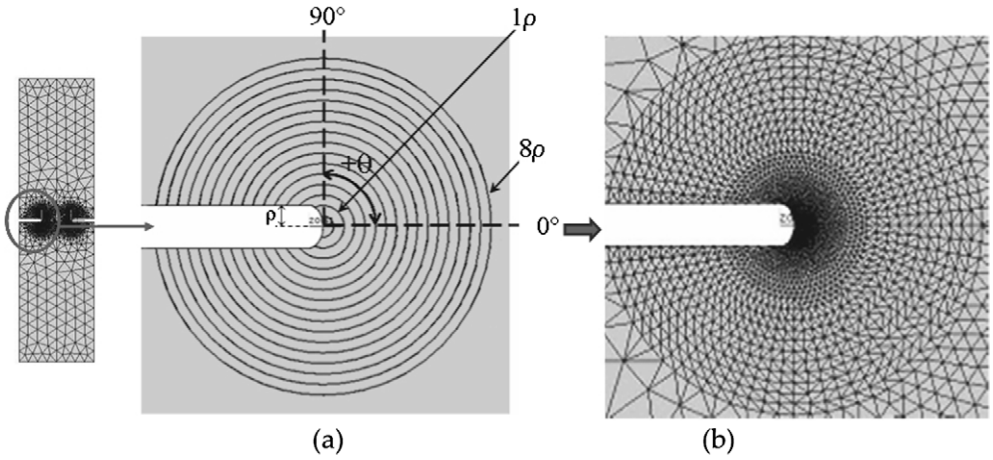

Fig. 4. (a) Radial and angular coordinates used for evaluating stress fields. (b) Close-up view of element sizing in the FE model for the specimen front plane in the vicinity of the left notch.

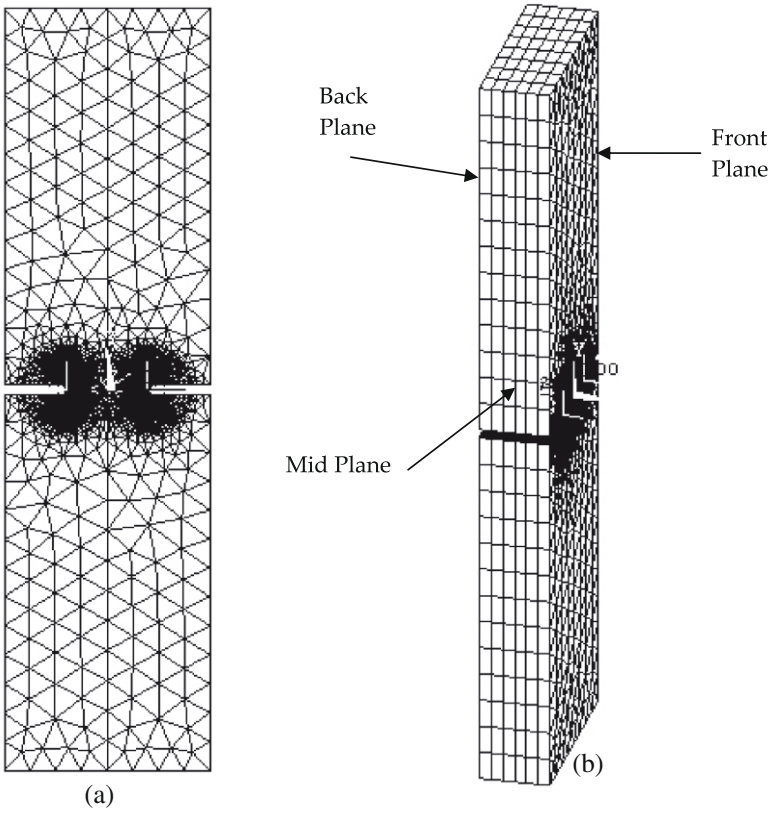

Fig. 5. (a) Front plane and (b) isometric view showing x–y-planes through the specimen thickness.

modeling of smooth cylindrical test specimens loaded in [001] direction. The notched test specimens used in this work are loaded in the [001] direction while three different secondary (notch) orientations are considered. Our observation of persistence of dominant slip systems, even at higher loads, in plastic zones of notched specimens, due to softening and slip localization in the superalloy tested, led us to conclude that we can extract useful information about evolution of plastic zones as a function of load and orientation, from elastic 3D FEA. This procedure is appropriate for the high strength superalloy tested that exhibits strong strain localization. This has immediate practical applica-

Table 2
Material properties used in the analysis of the notched single crystal specimens (Kalluri et al., 1991; Milligan and Antolovich, 1987).

Elastic modulus ($E_x = E_y = E_z$)	1.21×10^{11} Pa
Shear modulus ($G_x = G_y = G_z$)	1.29×10^{11} Pa
Poisson's ratio ($\nu_x = \nu_y = \nu_z$)	0.395
S_{11}	8.242×10^{-12}/Pa
S_{12}	-3.253×10^{-12}/Pa
S_{44}	7.752×10^{-12}/Pa
C_{11}	2.50×10^{11} Pa
C_{12}	1.63×10^{11} Pa
C_{44}	1.29×10^{11} Pa

Table 3
Slip plane and slip direction for the 12 octahedral slip systems.

Slip system	Slip plane ⟨1 1 0⟩{1 1 1}	Slip direction
1	(1 1 1)	[1 0 $\bar{1}$]
2	(1 1 1)	[0 $\bar{1}$ 1]
3	(1 1 1)	[1 $\bar{1}$ 0]
4	($\bar{1}$ 1 $\bar{1}$)	[1 0 $\bar{1}$]
5	($\bar{1}$ 1 $\bar{1}$)	[1 1 0]
6	($\bar{1}$ 1 $\bar{1}$)	[0 1 1]
7	(1 $\bar{1}$ $\bar{1}$)	[1 1 0]
8	(1 $\bar{1}$ $\bar{1}$)	[0 $\bar{1}$ 1]
9	(1 $\bar{1}$ $\bar{1}$)	[1 0 1]
10	($\bar{1}$ $\bar{1}$ 1)	[0 1 1]
11	($\bar{1}$ $\bar{1}$ 1)	[1 0 1]
12	($\bar{1}$ $\bar{1}$ 1)	[1 $\bar{1}$ 0]

tions to blade design for identifying critical cooling hole or other stress concentration locations in the blade that are most susceptible for fatigue crack initiation.

We present an experimental and numerical investigation to elucidate the initial evolution of plasticity and stress fields at a notch in a ductile cubic single crystal as a function of secondary orientation. We have chosen a Ni-base superalloy for experimental studies. Although this material consists of two phases (FCC γ-matrix and $L1_2$ γ'-precipitate), in the case where particle shearing takes place at room temperature, geometrically, plastic deformation is analogous to a single-phase FCC crystal. The γ' precipitate is an intermetallic. Consequently, these materials have a much higher critical resolved shear stress (CRSS) than pure Cu or Al. The advantage of using a superalloy crystal is that it yields at considerably high applied stresses and therefore the applied load levels at small plastic zones can be accurately controlled and measured. Three crystallographic orientations, designated as A, B and C, shown in Fig. 1, are considered in this research. The primary orientation (load direction) is [0 0 1] for all three orientations, however, the notch direction, and hence the nature of the face and the side planes, varies among the three orientations.

A 3D finite element model that incorporates elastic anisotropy was employed to predict the slip systems activated in the experimentally tested notched single crystals. We demonstrate that because of slip localization in the material tested, the meth-

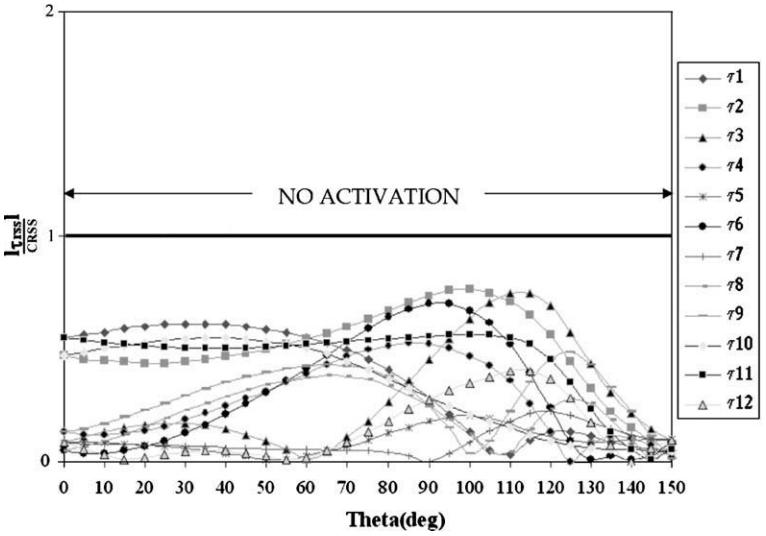

Fig. 6. Nondimensional RSS values at $r = 2\rho$ for orientation A at 1500 N load.

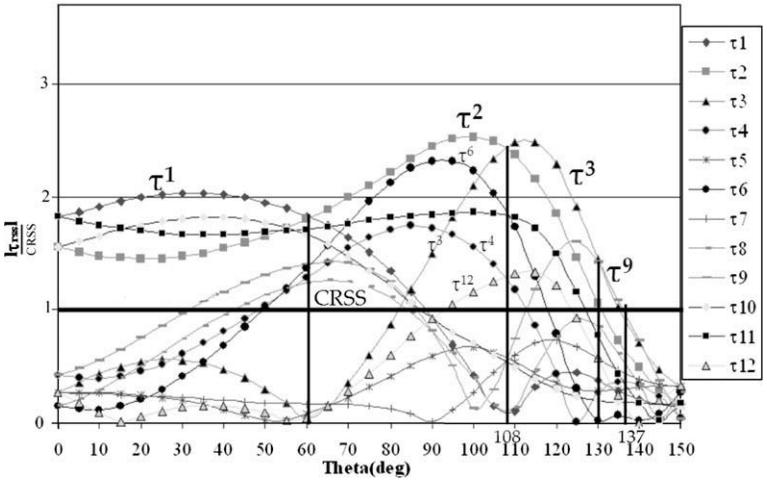

Fig. 7. Nondimensional RSS values at $r = 2\rho$ for orientation A at 4982 N load. The dominant slip systems are τ^1 from 0° to 60°, τ^2 from 60° to 108°, τ^3 from 108° to 130°, and τ^9 from 130° to 137°.

odology is capable of predicting the evolution of plasticity at relatively high load levels. It is shown that the inclusion of 3D analysis and elastic anisotropy are essential for evaluation of plasticity evolution at the surface and through the specimen thickness.

2. Material and experimental procedures

Single crystals of Ni-base superalloys were provided in as-heat-treated condition by Pratt and Whitney. The microstructure of the alloys consisted of cubical primary γ' precipitates in a matrix of solid solution γ. Both crystals did not have any noticeable eutectic pools or pores. Laue X-ray back-reflection technique was employed to identify the crystallographic orientations of them, based on which the samples' directions were realized.

Fig. 2 presents the geometry of the double-notched tensile samples used in this study. Front and back planes of the specimen are identified separately in Fig. 2 to facilitate the discussion of slip fields for specimens with an asymmetrical orientation. Electro-discharge machining (EDM) technique was employed to prepare dog-bone shaped un-notched samples. Then they were carefully polished on both faces and sides to remove any damage caused by EDM. Three sample orientations with notches parallel to the $[\bar{1}10]/[1\bar{1}0]$ (orientation A), $[010]/[0\bar{1}0]$ (orientation B), and $[\bar{3}10]/[3\bar{1}0]$ (orientation C) directions were prepared (see Fig. 1). Prior to the introduction of notches, X-ray analysis confirmed that all expected orientations were off by no more than 8°. We note that the [001] primary orientation direction in turbine blade castings is also controlled to within 8–10°. The notches were introduced using a slow speed saw with a thin diamond blade. A special fixture was designed to achieve co-planar notches with approximately equal lengths on both sides. We were able to produce consistent notch tips with careful and methodical procedures.

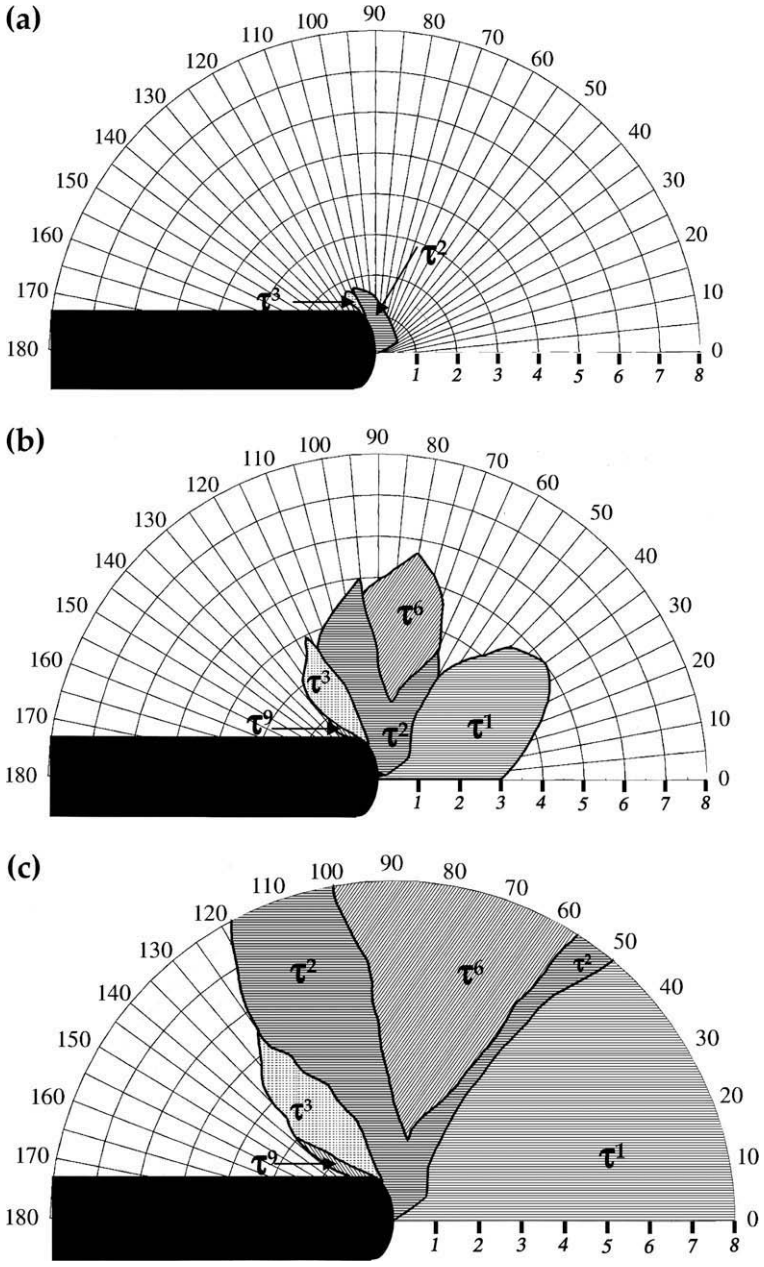

Fig. 8. Evolution of activated (dominant) slip systems around the notch for orientation A as a function of load: (a) 1600 N load ($K_I = 15\ \mathrm{MPa}\sqrt{\mathrm{m}}$), (b) 3200 N load ($K_I = 30\ \mathrm{MPa}\sqrt{\mathrm{m}}$), and (c) 4982 N load ($K_I = 50\ \mathrm{MPa}\sqrt{\mathrm{m}}$).

The yield stresses for the two crystals were evaluated by conducting tensile tests along the [001] direction using dog-bone samples with rectangular cross-sections. The analysis of deformation bands on the face and the sides of samples revealed that slip took place along the {111} planes (Ebrahimi et al., 2006; Westbrooke, 2005; Ebrahimi and Westbrooke, 2008). Assuming the activation of octahedral slip systems, the average CRSS values were measured to be 324 MPa and 378 MPa for crystals 1 and 2, respectively. We note that these CRSS values are about 30 times higher than for pure aluminum. Notched specimens with orientations A and B were machined from crystal 1, but the specimen with orientation C was cut from crystal 2.

In order to investigate the evolution of plasticity near notch tips, samples were loaded to various levels of apparent stress intensity factors (i.e. calculated based on the sharp crack isotropic assumption) in the range of $K_I = 20\ \text{MPa}\sqrt{\text{m}}$ to $50\ \text{MPa}\sqrt{\text{m}}$. The development of slip traces near the notches was recorded using optical microscopy.

3. Finite element analysis

A 3D linear elastic anisotropic finite element (FE) model, using commercial ANSYS FE software (version 8.1), was used for computing stress fields. Material (X,Y,Z) and specimen (X',Y',Z') coordinate systems were built as shown in Fig. 3. In this study the loading direction was the same for all samples and the rotation of the axis

Table 4
Comparison of numerical and experimental results for orientation A, at $r = 5\rho$.

Sector	Numerical solution			Experimental results	
	θ (°)	τ_{max}	Slip system	θ (°)	Slip plane
I	0–56	τ^1	(1 1 1) [1 0 $\bar{1}$]	0–75	(1 1 1)
II	56–60	τ^2	(1 1 1) [0 $\bar{1}$ 1]		
III	60–95	τ^6	($\bar{1}$ 1 $\bar{1}$) [0 1 1]	75–108	($\bar{1}$ 1 $\bar{1}$)
IV	95–125	τ^2	(1 1 1) [0 $\bar{1}$ 1]	96–117	(1 1 1)
V	125–127	τ^3	(1 1 1) [1 $\bar{1}$ 0]		

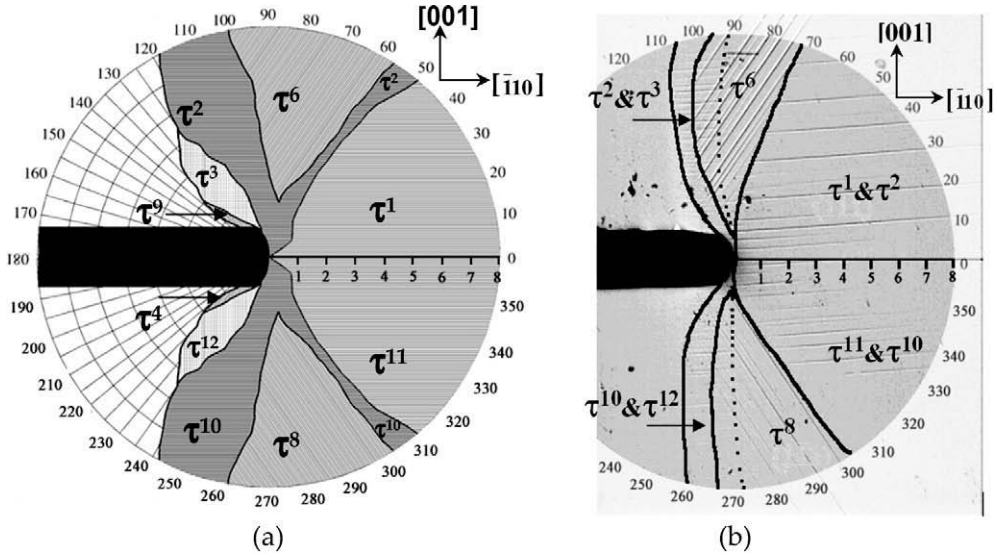

Fig. 9. Comparison between numerical and experimental results for orientation A at load = 4982 N. (a) Numerically generated slip fields. (b) Experimentally observed slip fields.

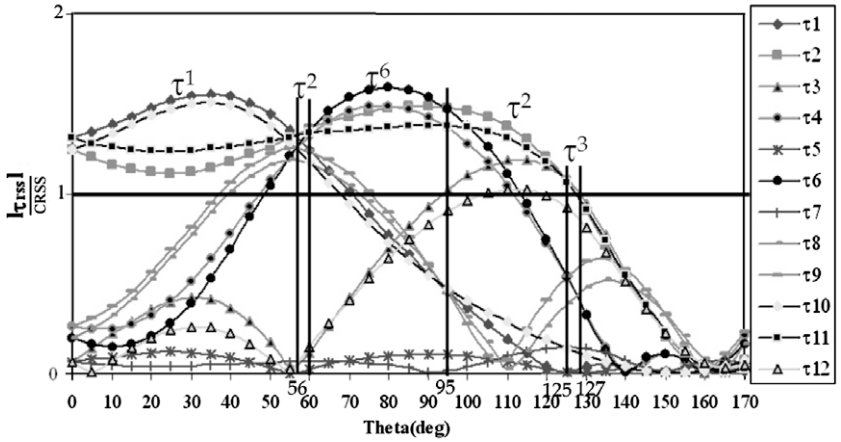

Fig. 10. RSS values and dominant slip systems predicted at $r = 5\rho$ for orientation A at 4982 N load.

could be simply defined by angle β. Owing to the fourfold symmetry of the loading axis, the secondary orientation repeats after a 90° rotation. Furthermore, since the notch plane is the (001) plane, there is a mirror symmetry about the notch plane for all orientations considered. Secondary orientations selected and their crystallographic symmetry is described below.

(a) *Orientation A:* Secondary orientation of $\beta = 45°$ is selected for which notches are parallel to the $[\bar{1}10]/[1\bar{1}0]$ directions. This orientation has a twofold symmetry about the notch axis and there is a mirror symmetry about the mid-plane (perpendicular to the notch plane).
(b) *Orientation B:* Secondary orientation of $\beta = 0°$ is selected, which has a fourfold symmetry about the notch axis with mirror symmetry about the mid-plane. For this orientation notches are parallel to the $[010]/[0\bar{1}0]$ directions.
(c) *Orientation C:* Secondary orientation of $\beta = 72°$ is selected, for which the notches are parallel to the $[\bar{3}10]/[3\bar{1}0]$ directions. This orientation is not symmetrical about the notch direction and does not have mirror symmetry relative to the mid-plane, ((310) plane).

The specific specimen dimensions used for specimens A, B, and C in reference to Fig. 2 are given in Table 1. Fig. 4 shows a close-up view of the FE mesh at the left notch. The front plane has precise element sizing along defined radial lines around the notch tip at 5° intervals. The 3D SOLID95 (3D structural solid with 20 nodes) elements used are capable of incorporating anisotropic properties. To compute the stresses in the vicinity of the notch (radial and angular), 16 concentric circular arcs were created between the radii 0.5ρ to 8ρ in 0.5ρ increments, where ρ is the notch height (Fig. 2). The FE mesh allows stress data to be collected on seven x–y-planes through the specimen thickness, including the front, middle, and back planes (Fig. 5). The elastic properties of FCC crystals exhibit cubic symmetry

Table 5
Numerical predictions of dominant slip system sectors for orientation B.

Sector	$r = 1\rho$		$r = 2\rho$		$r = 3\rho$		$r = 4\rho$	
	θ (°)	τ_{max}	θ (°)	τ_{max}	θ (°)	τ_{max}	θ (°)	τ_{max}
I	0–50	τ^4	0–50	τ^4	5–50	τ^4	16–48	τ^4
II	50–110	τ^1	50–60	τ^{11}	50–68	τ^{11}	48–57	τ^{11}
III	–	–	60–65	τ^{10}	58–66	τ^{10}	57–65	τ^{10}
IV	–	–	65–132	τ^1	66–132	τ^1	65–127	τ^1
	$r = 5\rho$		$r = 6\rho$		$r = 7\rho$		$r = 8\rho$	
	θ (°)	τ_{max}	θ (°)	τ_{max}	θ (°)	τ_{max}	θ (°)	τ_{max}
I	24–46	τ^4	30–45	τ^4	85–102	τ^9	–	–
II	46–55	τ^{11}	45–50	τ^{11}	–	–	–	–
III	55–58	–	50–68	–	–	–	–	–
IV	58–63	τ^{10}	68–85	τ^{11}	–	–	–	–
V	63–121	τ^1	85–110	τ^4	–	–	–	–
VI	–	–	110–113	τ^{11}	–	–	–	–

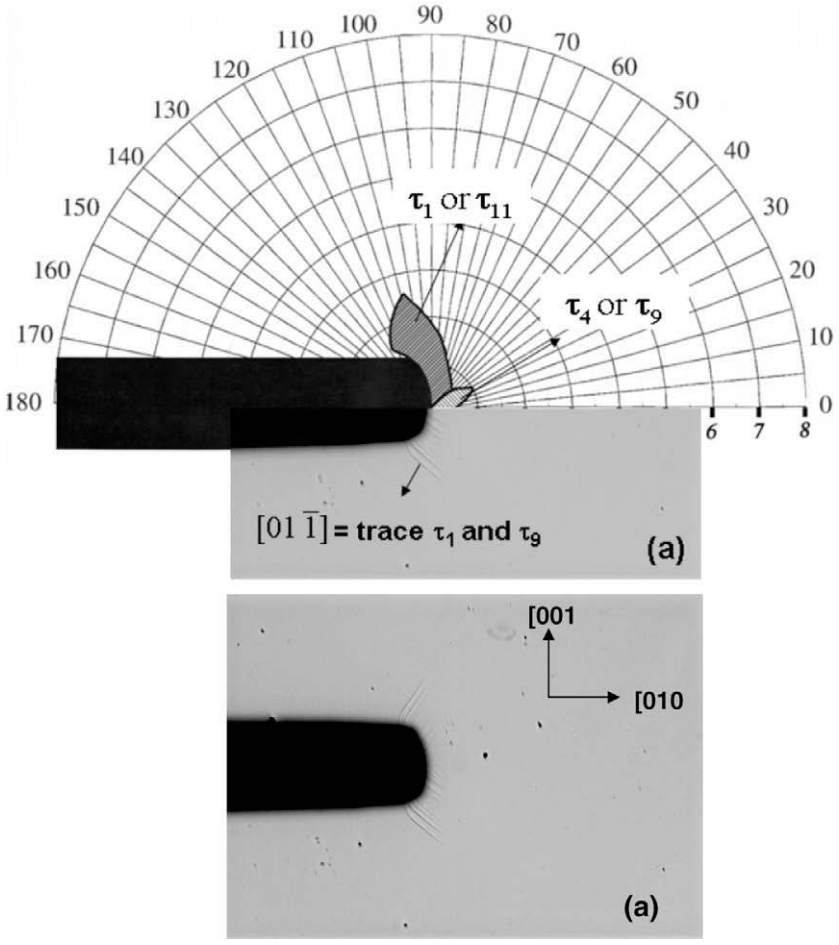

Fig. 11. Evolution of activated (dominant) slip systems around the notch for orientation B as a function of load: (a) 1780 N ($K_I = 20\ \mathrm{MPa}\sqrt{\mathrm{m}}$) and (b) 3456 N ($K_I = 45\ \mathrm{MPa}\sqrt{\mathrm{m}}$).

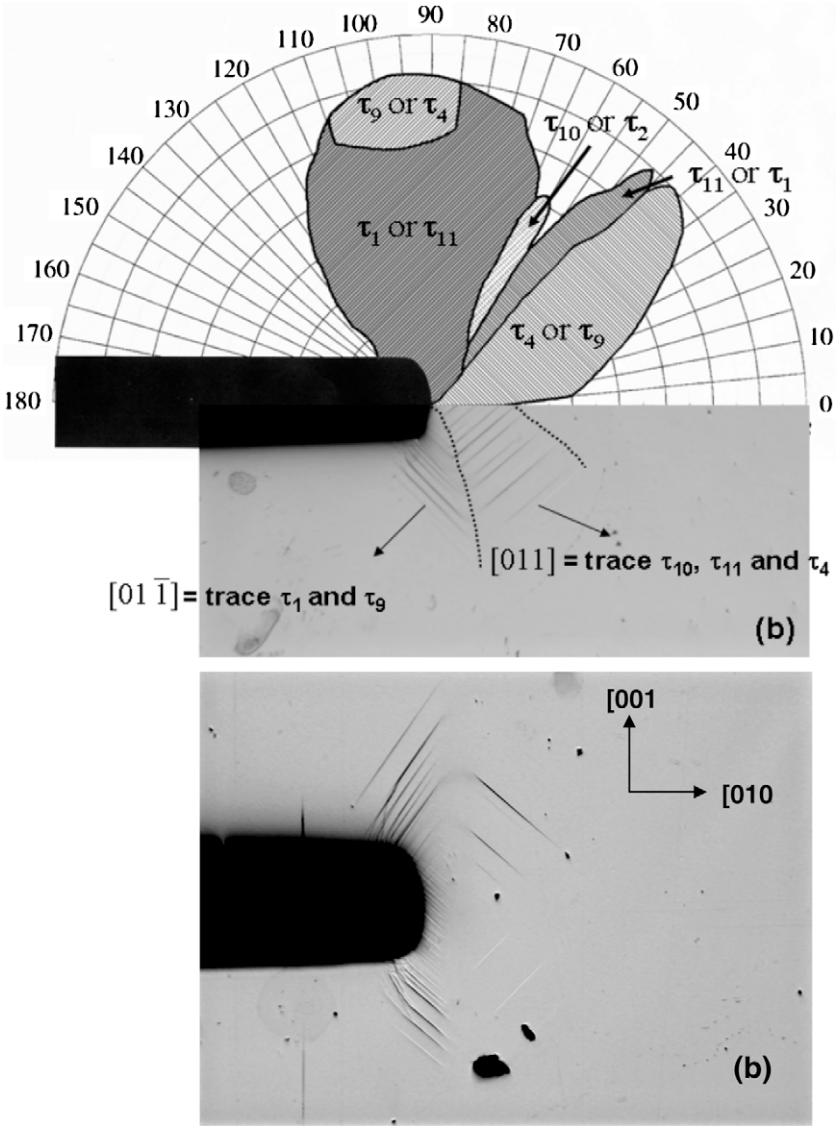

Fig 11. (*continued*)

and can be described by three independent elastic constants which are defined by either the elastic compliance values (S_{11}, S_{12}, S_{44}), the elastic stiffness values (C_{11}, C_{12}, C_{44}), or the elastic modulus (E), shear modulus (G) and Poisson's ratio (ν). (Lekhnitskii, 1963). Typically, the elastic compliance and stiffness constants are measured along the [001] primary orientation and relate to each other as follows: $C_{11} = (S_{11} + S_{12})/[(S_{11} - S_{12})(S_{11} + 2S_{12})]$, $C_{12} = -S_{12}/[(S_{11} - S_{12})(S_{11} + 2S_{12})]$, $C_{44} = 1/S_{44}$. Along the primary orientations, the elastic modulus $E = \{S_{11} - 2[(S_{11} - S_{12}) - S_{44}/2]\}^{-1}$, $G = 1/S_{44} = C_{44}$ and $\nu = -S_{12}/S_{11}$. Table 2 lists the elastic material properties used in the FE model (Kalluri et al., 1991; Milligan and Antolovich, 1987). The slip plane and slip direction for the 12 primary octahedral slip systems are given in Table 3. The component stresses at the FE nodal locations were transformed into 12 RSS components $(\tau^1 - \tau^{12})$ as defined in Table 3. These RSS values were plotted as a function of θ (from 0° to top of the notch) at 16 radii ranging from 0.5ρ to 8ρ in 0.5ρ intervals. These plots were created for each surface plane and were used to generate polar plots that depict the evolution of activated slip systems as a function of load.

4. Dominant slip systems

The yielding of single crystals is usually evaluated by Schmid's law, which states that plasticity in single crystals takes place when the shear stress resolved on a slip plane and in a slip direction reaches a critical value that is independent of the loading direction. Fig. 6 presents RSS values for the 12 systems as a function of θ angle for orientation A at 1500 N ($K_I = 14$ MPa$\sqrt{\text{m}}$) applied load. Since none of the RSS values exceeds the CRSS, no slip is expected to be activated at radius $r = 2\rho$ on the surface of this specimen. As load is increased, eventually slip will take place on the system with the highest RSS, which in this case would be the τ^2 system at about $\theta = 98°$. The initiation of plasticity is expected to modify the stress field from what is calculated based on the linear elastic approach. However, experimentally we observed that this modification is not significant and indeed the slip systems activated matched those predicted based on the FEA results. For example, Fig. 7 shows the RSS as a function of θ at 4982 N ($K_I = 50$ MPa$\sqrt{\text{m}}$). Experimental results revealed that indeed the slip systems with the highest RSS, i.e. τ^1, τ^2, τ^3 and τ^9 were activated, irrespective of the sequence of

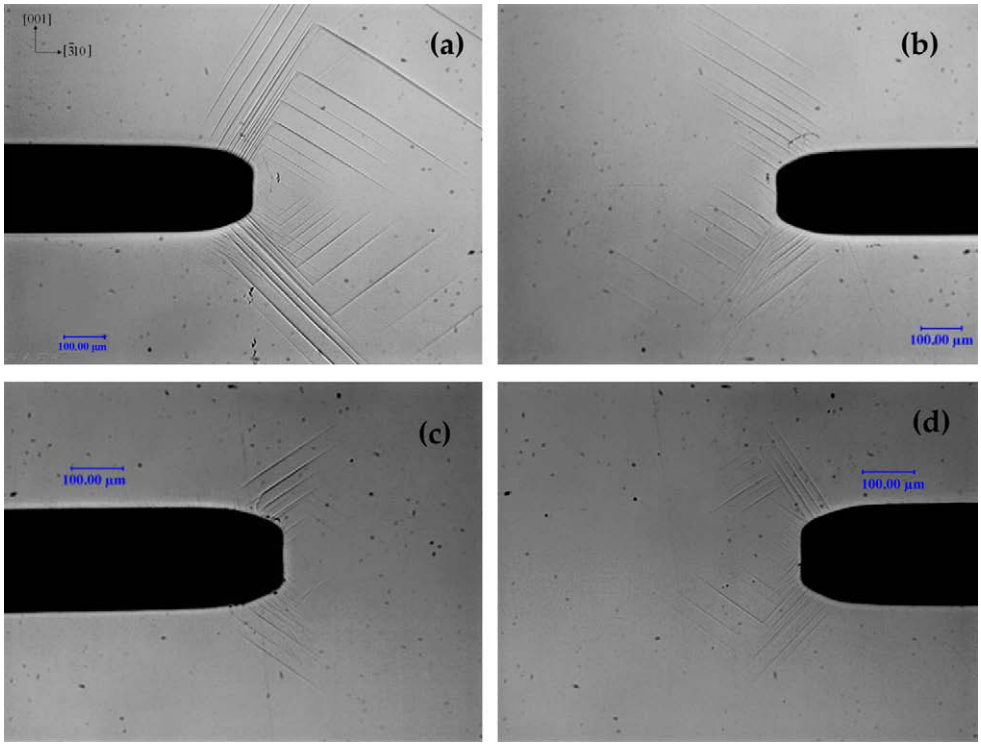

Fig. 12. Optical picture of deformation bands observed for orientation C at 3500 N load ($K_I = 30\ \mathrm{MPa}\sqrt{\mathrm{m}}$). (a) Front plane, left notch. (b) Front plane, right notch. (c) Back plane, right notch. (d) Back plane, left notch.

their activation. Each of these slip systems was activated first within their respective range of θ angle. Furthermore, it was noticed that when plasticity was initiated in a slip system at a given (r,θ), it persisted at higher load levels, i.e. no other slip system became activated at that point except at very large loads. This observation implies that as soon as plasticity is initiated the rate of increase in resolved shear stresses on the other slip systems will be reduced significantly. The persistence of slip can partially be attributed to the softening effect due to γ'-particle shearing in the superalloy studied here (Ebrahimi et al., 2006; Westbrooke, 2005).

Based on the above observations we define "*dominant slip systems*" as those slip systems that experience *initially* the highest RSS at a given radial and angular location near the notch. Therefore, for each point (r,θ) only one dominant slip system can be identified. Clearly, the elastic solution cannot account for nonlinear effects due to plasticity, however, our approach is very effective at identifying which slip system is activated initially at a given (r,θ), and because of persistence of activated slip systems in the superalloy used, we are able to predict slip evolution quite well at higher loads also. The high CRSS of these superalloys results in high elastic strains at yield. We acknowledge that higher elastic strains will create larger incompatibilities among the different slip systems. However, the evolution of the "dominant slip systems" as evaluated by this work is independent of the value of CRSS.

We define a sector as the domain where a particular slip system is "dominant" and the sector boundaries mark the transition from one dominant slip system to another. Using this process, dominant slip systems for $r = 0.5\rho$ to 8ρ in 0.5ρ intervals, as a function of θ for the three orientations tested were determined. As an example, Fig. 8 demonstrates the evolution of the dominant slip sectors as a function of load for orientation A in the form of polar plots around the notch.

5. Comparison of numerical and experimental results

5.1. Orientation A

Fig. 9 compares numerically generated and experimentally observed slip fields based on the dominant slip concept. The experimentally observed slip bands around the notch for orientation A, at load level of 4982 N ($K_I = 50\ \mathrm{MPa}\sqrt{\mathrm{m}}$), are shown in Fig. 9b. The slip bands show a slight asymmetry about the notch axis, which can be attributed to the crystallographic deviation from $\langle 1\,0\,0\rangle$ orientations as well as any misalignment in the loading fixture. Good agreement is seen between the experimentally observed slip bands and the trace of the dominant slip systems predicted. Except for small regions, consistent with the dominant slip approach, only one slip trace was observed in each sector.

For a detailed comparison of results at a specific radius, Fig. 10 shows RSS values as a function of θ for the 12 slip systems at radius $r = 5\rho$. The active dominant slip systems are found to be τ^1 from $\theta = 0^\circ$ to 56°, τ^2 from $\theta = 56^\circ$ to 60°, τ^6 from $\theta = 60^\circ$ to 95°, τ^2 again from $\theta = 95^\circ$ to 125°, and τ^3 from $\theta = 125^\circ$ to 127°. Table 4 compares the experimental and numerical sector boundaries at $r = 5\rho$. Slip traces related to the $(1\,1\,1)$ slip plane are activated from 0° to 75° on the experimental specimen whereas the numerical model predicts the slip systems τ^1 and τ^2 (related to the $(1\,1\,1)$ slip plane) are activated from 0° to 60°. Numerical analysis predicts the τ^6 system to be dominant between 60° and 95°, while the slip traces related with $(\bar{1}\,1\,\bar{1})$ slip plane extend from 75° to 108°. Experimental slip traces [$(1\,1\,1)$ slip plane] are observed from $\theta = 96^\circ$ to 117° while the numerical analysis predicts the activation of τ^2 and τ^3 from $\theta = 95^\circ$ to 127°. This analysis reveals that the numerical model predicts the development of the slip bands near the notch tip for specimen A to within 10°.

5.2. Orientation B

The slip fields activated at the surface for this orientation are very different from those observed for orientation A. Fig. 11 shows a comparison between numerically predicted and experimentally observed evolution of activated slip systems around the notch for two load levels. Because of the crystallographic symmetry of the specimen only domains for 180° are presented. At a lower load of 1780 N ($K_I = 20$ MPa$\sqrt{\text{m}}$), slip traces along $[0\,1\,\bar{1}]$ direction are activated, corresponding to $(1\,1\,1)$ or $(\bar{1}\,1\,1)$ slip planes (τ^1 and τ^9), as shown in Fig. 11a. Here τ^1 represents the dominant system for the bottom half (optical picture) and τ^9 to the top half of the specimen. At the higher load of 3456 N ($K_I = 45$ MPa$\sqrt{\text{m}}$), a second set of slip systems becomes activated at a larger distance from the notch tip, with slip traces along $[0\,1\,1]$ direction, corresponding to $(1\,1\,\bar{1})$ or $(1\,\bar{1}\,1)$ slip planes (τ^{10}, τ^{11} and τ^4), as shown in Fig. 11b. Good agreement is seen between the observed slip traces and those predicted by the FE calculations at both load levels. Again, consistent with the dominant slip approach, only one slip system was found to be activated in each sector. Table 5 summa-

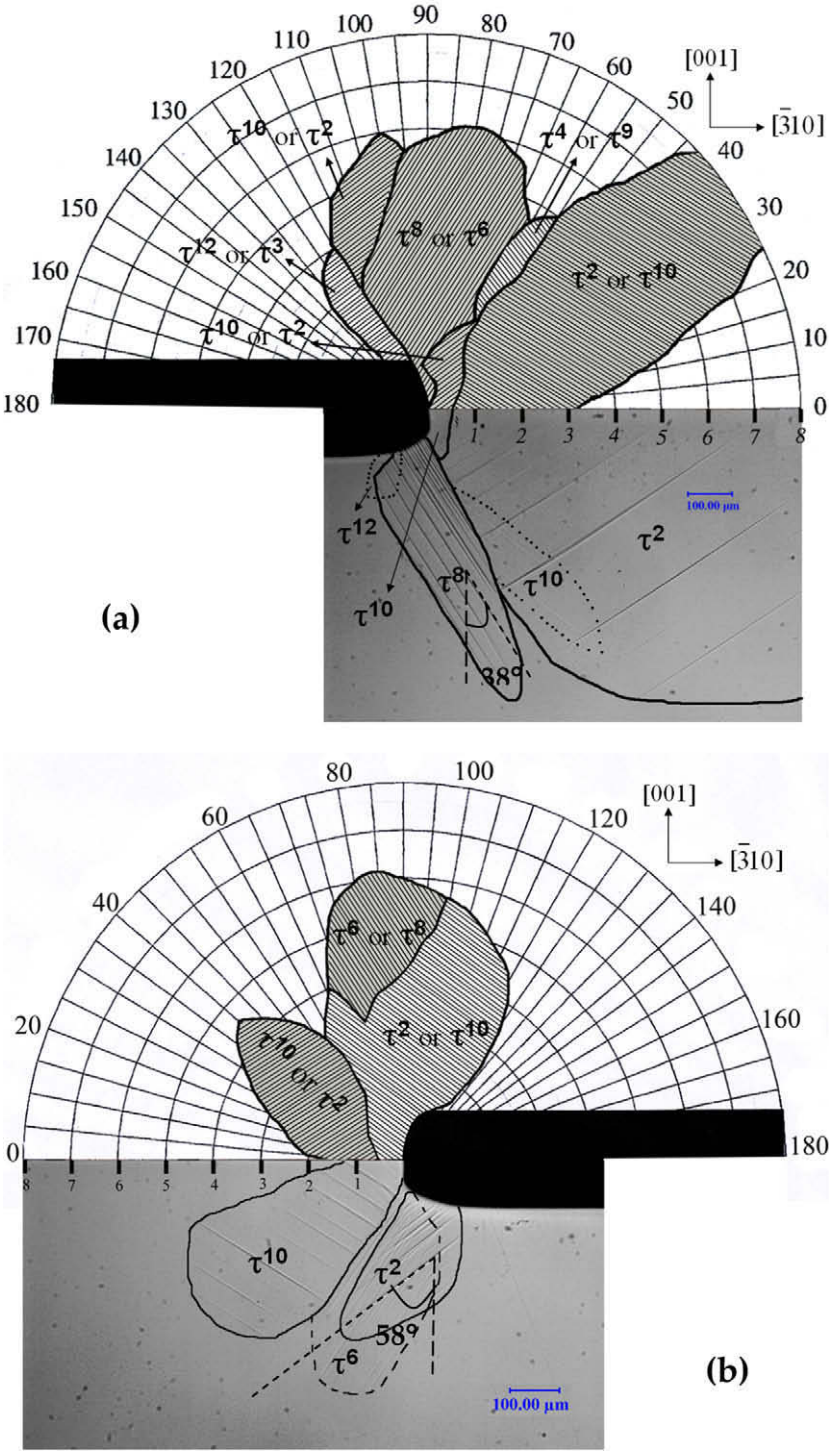

Fig. 13. Comparison between numerical and experimental results for orientation C loaded to 3500 N ($K_I = 30$ MPa$\sqrt{\text{m}}$). (a) Left notch and (b) right notch.

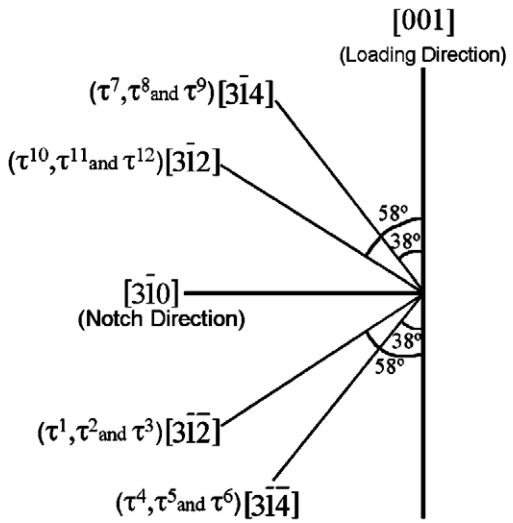

Fig. 14. Traces of different {1 1 1} slip planes on the surface of orientation C specimen [(1 3 0) plane].

rizes the numerical prediction of the dominant slip systems for orientation B.

5.3. Orientation C

Optically observed slip bands around the notch for orientation C, for front plane of left and right notches, are shown in Fig. 12. These pictures affirm the concept of the dominant slip by showing mostly one activated slip band in each sector. Note that "right" and "left" are defined based on looking at the front face. This orientation has mirror symmetry with respect to the notch plane, i.e. (0 0 1) plane, and consistently it exhibits symmetrical plastic zone on top and bottom half of the specimen. However, the crystallographic orientations around left and right notches are different and therefore the plastic zones in the vicinity of them are anticipated to be different.

Fig. 13 presents a comparison of the experimental and numerical slip fields at the left and right notches for orientation C, at a load level of 3500 N. To facilitate this comparison, Fig. 14 shows traces of different {1 1 1} slip planes on the plane of observation (that is the (1 3 0) plane). Similar to orientation B, two slip systems are mentioned in each sector of the numerically predicted slip field: the first represents the dominant system for the bottom half, corresponding to the optical picture and the second corresponds to the top half. The comparison reveals that the slip fields between the experimental and numerical results match relatively well at the right notch (Fig. 13a), except for the overlap of τ^2 and τ^6 systems in a region near the notch. However, a discrepancy is seen at the left notch (Fig. 13a) where the numerical results predict τ^4 to be dominant between τ^2 and τ^8 (and τ^9 to be dominant between τ^8 and τ^{12}), but τ^4 and τ^9 were not seen in the experimental results. The domains of τ^2, τ^1 (near the notch), and τ^8 and τ^{12} at the left notch, and the domains of τ^1, τ^2 and τ^6 at the right notch were correctly predicted by the numerical results. Furthermore, the plastic zone sizes predicted by the numerical results show good agreement with the experimental results at both notches. The good agreement between the numerical and experimental results for orientation C, with asymmetric slip fields at both notches, lends further credence to the concept of dominant slip systems accurately predicting the onset and evolution of slip systems as a function of load in triaxial stress fields.

6. Effect of elastic anisotropy

To demonstrate the importance of including elastic anisotropy for accurate prediction of plasticity evolution in triaxial stress fields, we compare anisotropic and isotropic analysis results. We

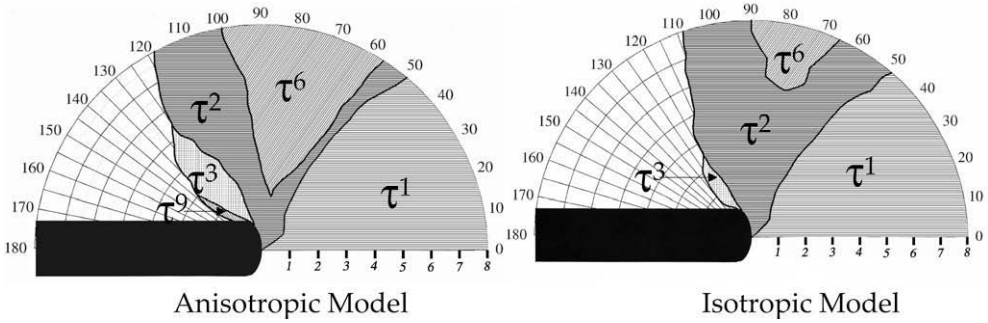

Fig. 15. Comparison between the anisotropic and isotropic slip fields for orientation A, at 4982 N load. (a) Anisotropic model and (b) isotropic model.

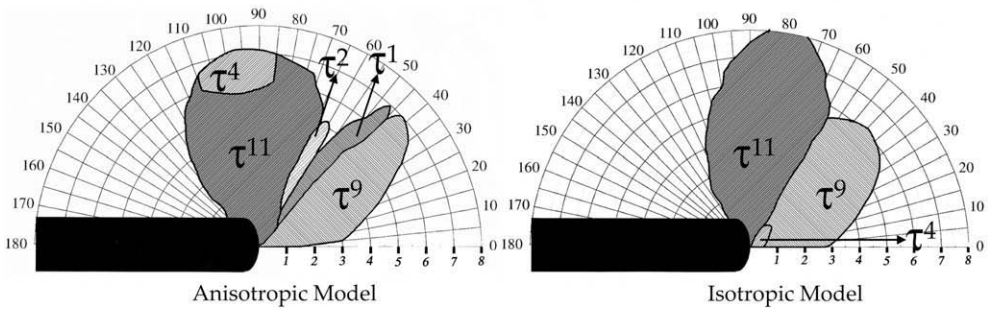

Fig. 16. Comparison between the anisotropic and isotropic slip fields for orientation B, at 4982 N load. (a) Anisotropic model and (b) isotropic model.

used Hashmin and Shtrikman's (1962a,b) method for calculating the isotropic properties for our model by taking the arithmetic average of their proposed upper and lower bounds to get the elastic modulus, $E = 2.39 \times 10^{11}$ Pa and shear modulus, $G = 0.8354 \times 10^{11}$ Pa.

Fig. 15 compares the isotropic and anisotropic results for orientation A at 4982 N load. The maximum RSS is higher in the isotropic material. The incorporation of anisotropy modified the slip sector boundaries. While the area covered by τ^1 is nearly identical in both specimens, the slip sector boundaries for τ^2, τ^3, and τ^6 are dissimilar. Additionally, τ^9 was dominant only in the anisotropic case. More importantly, the anisotropic slip field for τ^6 is very similar to the experimentally observed slip field.

Fig. 16 shows the comparison between anisotropic and isotropic slip fields for orientation B, at a 4982 N load. The anisotropic and isotropic results are markedly different. The comparison shows that the incorporation of anisotropy not only modifies the boundaries of the dominant slip systems, but also changes the number of dominant slip systems.

Fig. 17 compares anisotropic and isotropic slip fields for the left notch (front plane) for orientation C, at a 3500 N load. Again, the incorporation of anisotropy is seen to significantly modify dominant slip system sector boundaries and also introduce additional slip systems. The plastic zone sizes are also seen to be markedly different. Similarly, a strong effect was observed when the effect was studied for the right notch.

These results demonstrate that inclusion of elastic anisotropy is important for accurately predicting activated slip systems in triaxial stress fields.

7. Comparison of results for materials with low CRSS

The single crystal turbine blade superalloy tested has a high CRSS value of 378 MPa, which is nearly 30 times higher than that

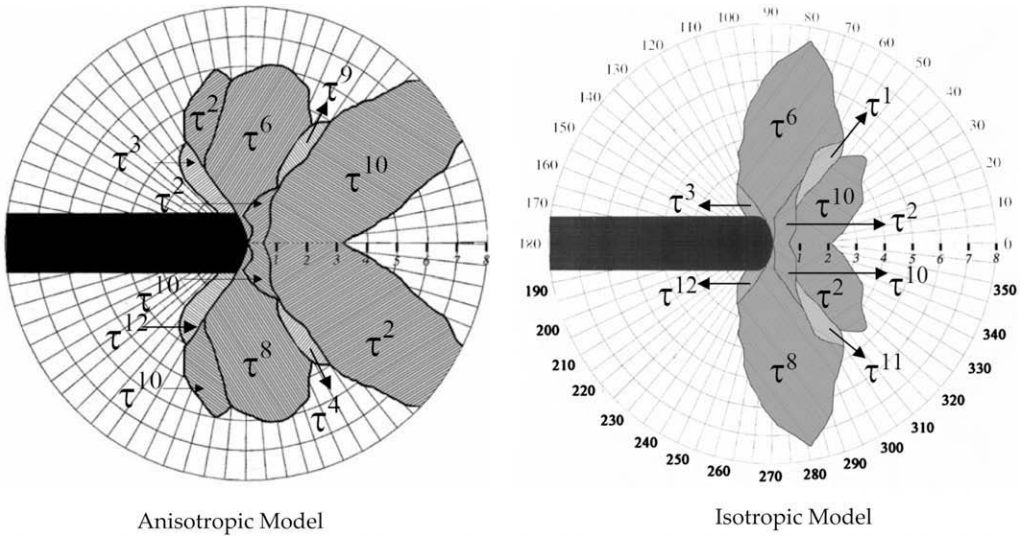

Fig. 17. Comparison between the anisotropic and isotropic slip fields for left notch (front plane), for orientation C, at 3500 N load.

Table 6
Comparison between experimental, numerical and analytical sector boundaries at $r = 0.35$ mm for orientation I in Crone et al. (2004).

Sector	Experimental		Numerical (based on dominant slip systems)		Analytical (Rice solution)
	θ (°)	Slip systems	θ (°)	Slip systems	θ (°)
1	0–32	τ^7, τ^8, τ^9, τ^1, τ^{11} or τ^{12}	0–26	τ^1	54.7
2	32–50	τ^4, τ^5 or τ^6	26–55	τ^5	90
3	50–97	τ^1, τ^2 or τ^3	55–100	τ^3	125.3
4	97–120	No activation	100–120	τ^9	–
5	120–150	τ^7, τ^8, τ^9, τ^1, τ^{11} or τ^{12}	120–165	τ^8	–
6	150–170	No activation	165–170	τ^7	–

Table 7
Comparison between experimental, numerical and analytical sector boundaries at $r = 0.7$ mm for orientation I in Crone et al. (2004).

Sector	Experimental		Numerical (based on dominant slip systems)		Analytical (Rice solution)
	θ (°)	Slip systems	θ (°)	Slip systems	θ (°)
1	0–33	τ^7, τ^8, τ^9, τ^1, τ^{11} or τ^{12}	0–32	τ^1	54.7
2	33–54	τ^4, τ^5 or τ^6	32–63	τ^5	90
3	54–102	τ^1, τ^2 or τ^3	63–110	τ^3	125.3
4	102–121	No activation	110–132	τ^9	–
5	121–152	τ^7, τ^8, τ^9, τ^1, τ^{11} or τ^{12}	132–170	τ^8	–
6	152–170	No activation	–	–	–

for pure aluminum. We have noted that the advantage of using a superalloy crystal is that it yields at considerably high applied stress and therefore the applied load levels at small plastic zones can be accurately controlled and measured. We also note that the evolution of the "dominant slip systems" as defined by this work is independent of the value of CRSS. The anisotropy ratio $(C_{11} - C_{12})/2C_{44}$ for the superalloy tested is 0.337, indicating pronounced elastic anisotropy. For copper this ratio is 0.31, also indicating pronounced elastic anisotropy. This ratio is 0.81 for aluminum, which is nearly isotropic. The elastic anisotropy governs the way the elastic stress field develops and hence also controls which slip systems become initially dominant in the triaxial stress field. To emphasize the point that elastic anisotropy matters, and not CRSS, we present simulations of careful experiments of plastic slip for FCC copper single crystal notches conducted by Crone et al. (2004). We have noted earlier that these orientations were analytically investigated by Rice (1987) (orientation I: [0 1 0] load and $[[1\,0\,\bar{1}]]/[\bar{1}\,0\,\bar{1}]$ notch directions, orientation II: [1 0 1] load and $([0\,1\,0]/[1\,0\,\bar{1}])$ notch directions). The material properties used are: $E = E_x = E_y = E_z = 6.7 \times 10^{10}$ Pa, $G = G_x = G_y = G_z = 7.5 \times 10^{10}$ Pa, and $v = v_x = v_y = v_z = 0.4161$. The load level chosen is arbitrary since our analysis is elastic. The FE model for the four-point bend specimen in Crone et al. (2004) was created analogous to the tensile specimen and RSS values as functions of θ for the 12 slip systems at $r = 0.35$ mm and $r = 0.7$ mm, respectively, were computed for orientation I. Tables 6 and 7 summarize the comparisons between experimental and numerical results at $r = 0.35$ mm and $r = 0.7$ mm for orientation I. The experimental results for the first three sectors match well with the numerical predictions, at $r = 0.35$ mm and $r = 0.7$ mm. Experimental results show two sectors with no slip activity. The numerical results do predict slip activity in these sectors. It is possible that these effects are due to slight discrepancies in material and load orientations. Activation of slip systems τ^9, τ^8 and τ^7 from $\theta = 100°$ to $170°$ are predicted correctly. Furthermore, both the experimental and numerical results indicate that the same slip systems (τ^1, τ^5, τ^3, τ^9 and τ^8) are activated at both $r = 0.35$ mm and $r = 0.7$ mm. We note that our approach of identifying "dominant slip systems" is effective in identifying activated slip systems in a copper single crystal notch.

8. Thickness effect

Because the notch stress field is strongly three dimensional we should expect a variation in the activated slip systems from the specimen surface to mid-thickness. Indeed, we see that the acti-

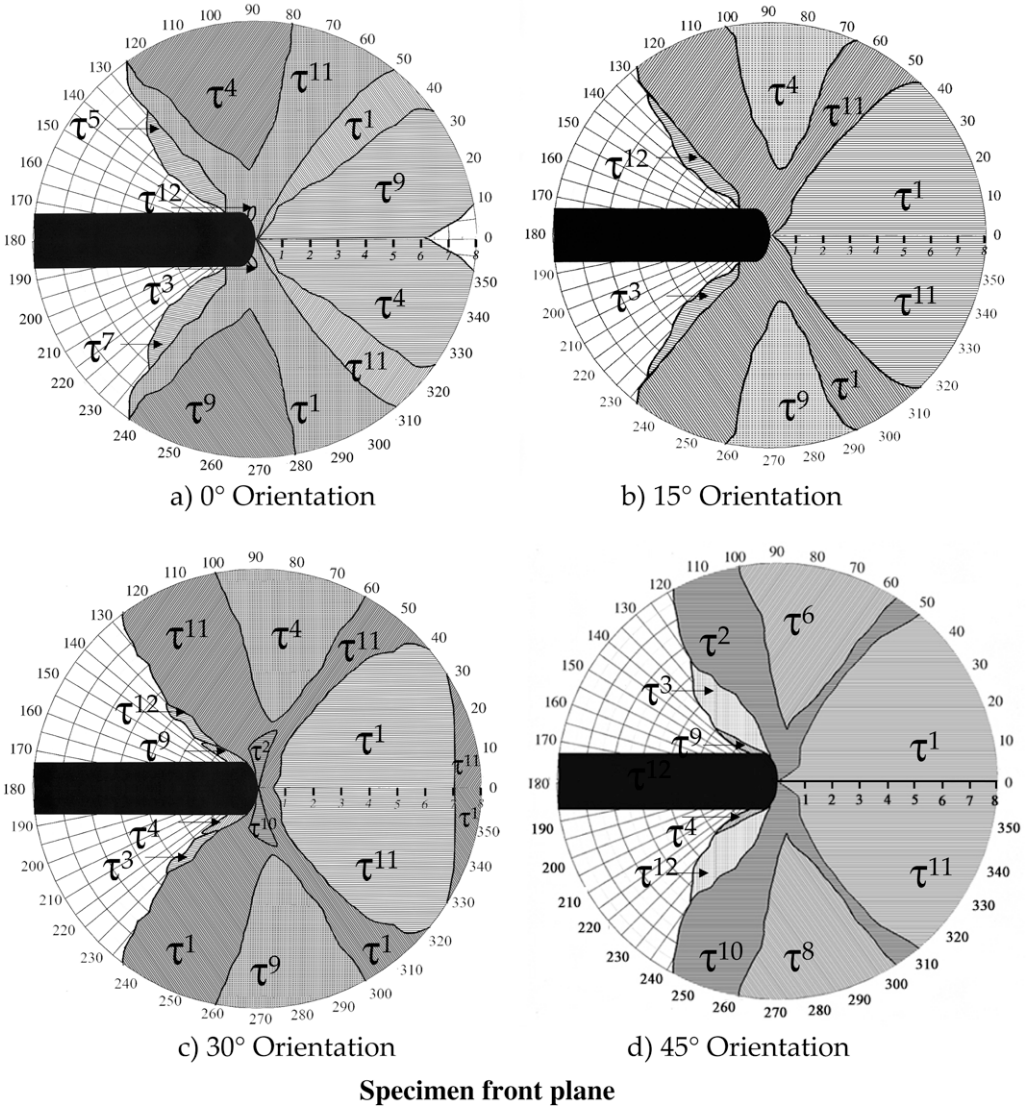

Fig. 18. Evolution of slip fields as a function of the secondary orientation on the front surface of the specimen around the left notch at 4982 N load.

vated slip systems are a strong function of through thickness location and secondary orientation. Flouriot et al. (2003) also show that there are strong differences between the crack tip plastic strain fields observed at the surface and mid-section of CT specimen tested, using EBSD and finite element analysis. The analysis was conducted at front and back planes and five interior x–y-planes through the specimen 0.3 mm apart (Fig. 5b). The secondary orientation was varied in 15° increments, from 0° to 45°, keeping the primary (load) orientation fixed along [0 0 1] direction. Figs. 18–20 illustrate the evolution of plasticity at the left notch, for front plane, 0.3 mm and 0.9 mm (mid plane), from front plane, respectively. The slip sector boundaries are seen to have complex shapes varying significantly as a function of both secondary orientation and through-thickness location. Fig. 19 shows a significant change in the activated slip systems and sector boundaries, even though it is only 0.3 mm from the free surface. The slip systems occur in pairs for $\beta = 0°$ and 45° at the midplane, shown in Fig. 20a and d, i.e. two dominant slip systems are active simultaneously over the entire midplane surface. Also, the slip sector boundaries for all four orientations appear very similar at the midplane. This outcome suggests that once generalized plane strain conditions are reached at the midplane, the secondary orientation dependence is minimized, for [0 0 1] loading.

One of the implications of variations in dominant slip systems and the maximum RSS through thickness is that fatigue crack initiation can be strongly dependent on the secondary orientation. Nalla et al. (2002) have indicated that important factors playing an important role in fatigue crack nucleation are the magnitudes of RSS on the slip planes and the normal stress on the slip plane that is initially activated. The variation of activated slip systems through the thickness implies that the load level that induces plasticity and its location vary as a function of crystallographic orientation. The magnitude of normal stress on that plane will also influence crack nucleation. Assuming that fatigue cracks start on the surface of the notch, specific locations along the notch were identified with the node numbering shown in Fig. 21. Since the analysis is linear, applied load is scaled such that the ratio of RSS/CRSS at a nodal point is equal to one where yielding is initiated, Tables 8–11 highlight the magnitude and location of maximum RSS and normal stress on the notch surface, as a function of secondary orientation and distance from front surface. These data can elucidate possibly on which slip plane and at which location fatigue crack may be initiated. Yielding is predicted to be initiated at the load level of 558 N for $\beta = 30°$ followed by 572 N load for $\beta = 15°$ at the same nodal point and thickness location (Tables 9 and 10). However, the

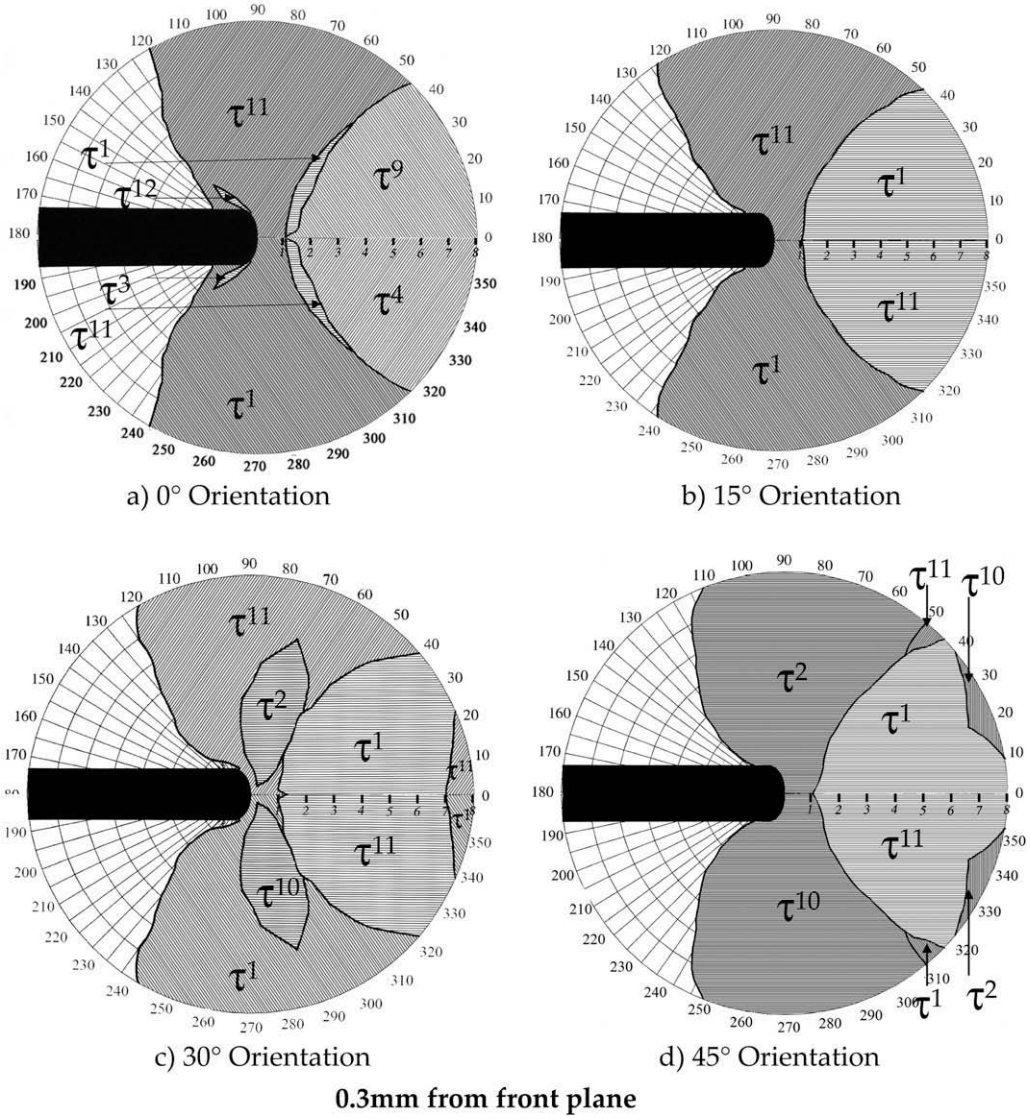

Fig. 19. Evolution of slip fields as a function of the secondary orientation at 0.3 mm from front surface around the left notch at 4982 N load.

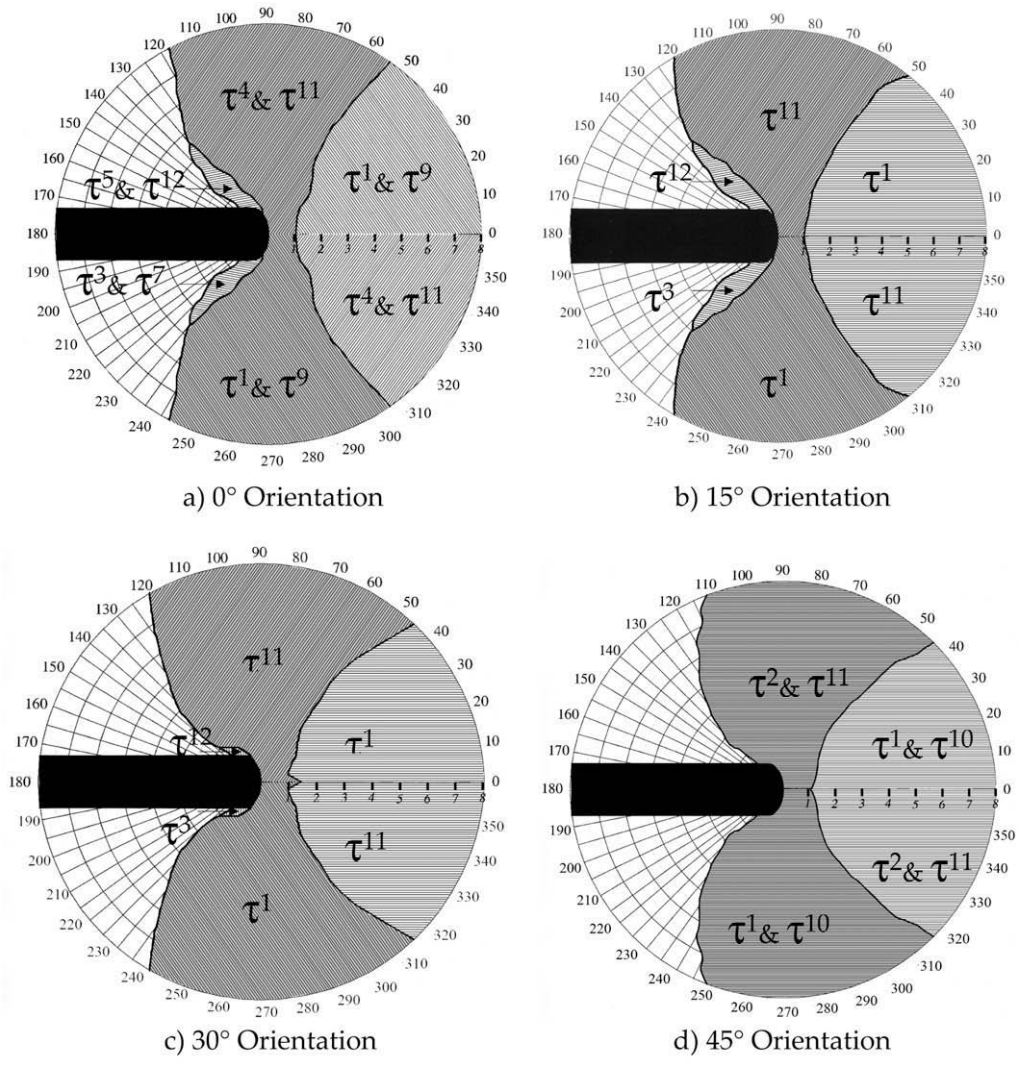

Fig. 20. Evolution of slip fields as a function of the secondary orientation at midplane (0.9 mm from front surface) around the left notch at 4982 N load.

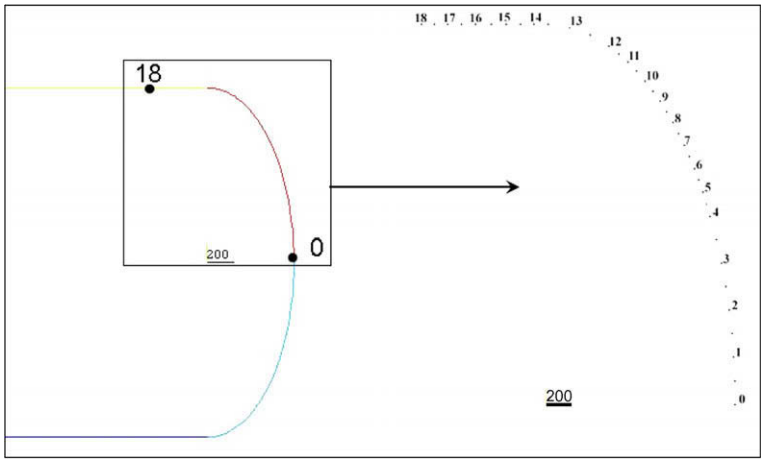

Fig. 21. Node numbering to locate specific points along the specimen notch.

Table 8
Maximum ratio of RSS/CRSS and the corresponding normal stress as a function of through-thickness axial location at the load where plasticity is initiated (612 N), for $\beta = 0^\circ$ secondary orientation.

Axial location from front surface (in mm)	Nodal location on the notch surface (Fig. 21)	Slip system	RSS/CRSS	Corresponding value of normal stress (MPa)
0	10	τ^{11}	0.844	414
0.3	**10**	τ^{11}	**1.0**	**709**
0.6	10	τ^{11}	0.983	777
0.9	10	τ^{4}, τ^{11}	0.970	802
1.2	10	τ^{4}	0.983	777
1.5	**10**	τ^{4}	**1.0**	**709**
1.8	10	τ^{4}	0.844	414

Table 9
Maximum ratio of RSS/CRSS and the corresponding normal stress as a function of through-thickness axial location at the load where plasticity is initiated (572 N), for $\beta = 15^\circ$ secondary orientation.

Axial location from front surface (in mm)	Nodal location on the notch surface (Fig. 21)	Slip system	RSS/CRSS	Corresponding value of normal stress (MPa)
0	11	τ^{11}	0.759	259
0.3	11	τ^{12}	0.939	504
0.6	11	τ^{12}	0.968	581
0.9	11	τ^{12}	0.982	620
1.2	11	τ^{12}	0.996	646
1.5	**11**	τ^{12}	**1.0**	**663**
1.8	9	τ^{4}	0.840	459

Table 10
Maximum ratio of RSS/CRSS and the corresponding normal stress as a function of through-thickness axial location at the load where plasticity is initiated (558 N), for $\beta = 30^\circ$ secondary orientation.

Axial location from front surface (in mm)	Nodal location on the notch surface (Fig. 21)	Slip system	RSS/CRSS	Corresponding value of normal stress (MPa)
0	11	τ^{11}	0.726	171
0.3	11	τ^{12}	0.850	328
0.6	11	τ^{12}	0.899	384
0.9	11	τ^{12}	0.932	414
1.2	11	τ^{12}	0.963	436
1.5	**11**	τ^{12}	**1.0**	**455**
1.8	11	τ^{12}	0.932	399

Table 11
Maximum ratio of RSS/CRSS and the corresponding normal stress as a function of through-thickness axial location at the load where plasticity is initiated (612 N), for $\beta = 45^\circ$ secondary orientation.

Axial location from front surface (in mm)	Nodal location on the notch surface (Fig. 21)	Slip system	RSS/CRSS	Corresponding value of normal stress (MPa)
0	**11**	τ^{3}	**1.0**	**293**
0.3	11	τ^{3}	0.962	316
0.6	11	τ^{3}	0.925	314
0.9	11	τ^{3}, τ^{12}	0.898	307
1.2	11	τ^{12}	0.925	314
1.5	11	τ^{12}	0.962	316
1.8	**11**	τ^{12}	**1.0**	**293**

normal stress for $\beta = 15^\circ$ is 663 MPa, considerably higher than 455 MPa for $\beta = 30^\circ$. Since the load levels to initiate yield (558 N and 572 N) are nearly the same, we can argue that the likelihood for fatigue crack nucleation is highest for $\beta = 15^\circ$ followed by $\beta = 30^\circ$. Tables 8 and 11 show that yielding is initiated at 612 N load level, simultaneously at two different axial locations, for both $\beta = 0^\circ$ and $\beta = 45^\circ$. Although the load level to initiate yield is the same for these two orientations, the normal stress for $\beta = 0^\circ$ is 709 MPa, much higher than 293 MPa for $\beta = 45^\circ$. We can conclude from this simplified analysis that $\beta = 45^\circ$ has the highest resistance to fatigue crack nucleation, followed by $\beta = 0^\circ$, $\beta = 30^\circ$ and $\beta = 15^\circ$. A study of effect of crystallographic orientation on fatigue failure of single crystal superalloy turbine blades by Arakere and Swanson (2002) also concluded that $\beta = 45^\circ$ had the highest resistance to fatigue failure, with loading in the $\langle 001 \rangle$ direction.

9. Summary

A comprehensive numerical and experimental investigation of evolution of plasticity near a notch in a superalloy single crystal is presented. The following are the important concepts and results gathered from our investigation:

(a) A 3D linear elastic *anisotropic* stress solution can predict the onset of yield and identify which slip system is activated initially at a given (r, θ) from the notch tip, and because of the persistence of activated slip systems, due to softening and slip localization, we are able to predict slip evolution quite well at higher loads also.
(b) The concept of "dominant slip system" defined as the slip system that initially experiences the highest RSS at a given location near the notch, is introduced. These slip systems persist at higher applied load levels.
(c) A sector is defined as the domain where a particular slip system is "dominant" and the sector boundaries mark the transition from one dominant slip system to another.
(d) The dominant slip systems are shown to accurately predict the evolution of activated slip sectors and sector boundaries observed experimentally, as functions of load and secondary orientation.
(e) The nature of elastic anisotropy, governed by the three independent constants E, ν and G (or stiffness constants C_{11}, C_{12}, and C_{44}, or compliance constants, S_{11}, S_{12}, and S_{44}), is important and not CRSS. The elastic anisotropy governs the way the elastic stress field develops and hence controls which slip systems become initially dominant/activated in the triaxial stress field.
(f) Comparison between the anisotropic and isotropic results shows that the incorporation of elastic anisotropy has a noticeable effect on the slip evolution at discontinuities. The incorporation of anisotropy not only modifies the boundaries of the dominant slip systems, but also changes the number of dominant slip systems.
(g) The activated slip systems are a strong function of both secondary orientation and through thickness location.
(h) Both numerical and experimental findings indicate that the slip sectors' boundaries have complex curved shapes rather than straight radial lines predicted by Rice's (1987) asymptotic solution.

Results shed light on the likelihood of fatigue crack nucleation and its location as a function of secondary crystallographic orientation.

Acknowledgments

The authors would like to thank Dr. Gregory R. Swanson at the NASA Marshall Space Flight Center, Huntsville, AL, for partial support of this work. The authors would also like to thank Dan Deluca

at Pratt & Whitney, East Hartford, CT, for supplying the superalloy single crystal.

References

Arakere, N.K., Swanson, G.R., 2002. Effect of crystal orientation on fatigue failure of single crystal nickel base turbine blade superalloys. ASME Journal of Gas Turbines and Power 124, 161–176.

Arakere, N.K., Siddiqui, S., Magnan, S., Ebrahimi, F., Forero, L., 2005. Investigation of three dimensional stress fields and slip systems for fcc single-crystal superalloy notched specimens. ASME Journal of Gas Turbines and Power 127 (3), 629–637.

Crone, W.C., Shield, T.W., 2001. Experimental study of the deformation near a notch tip in copper and copper–beryllium single crystals. Journal of the Mechanics and Physics of Solids 49, 2819–2838.

Crone, W.C., Shield, T.W., Creuziger, A., Henneman, B., 2004. Orientation dependence of the plastic slip near notches in ductile FCC single crystals. Journal of the Mechanics and Physics of Solids 52, 85–112.

Cuitino, A., Ortiz, M., 1996. Three-dimensional crack tip fields in four-point bending copper single-crystal specimens. Journal of the Mechanics and Physics of Solids 44 (6), 863–904.

Deluca, D., Annis, C., 1995. Fatigue in single crystal superalloys. Office of Naval Research, FR23800.

Drugan, W.J., 2001. Asymptotic solutions for tensile crack tip fields without kink-type shear bands in elastic-ideally plastic single crystals. Journal of the Mechanics and Physics of Solids 49 (9), 2155–2176.

Dunne, F.P.E., Wilkinson, A.J., Allen, R., 2007. Experimental and computational studies of low cycle fatigue crack nucleation in a polycrystal. International Journal of Plasticity 23, 273–295.

Ebrahimi, F., Westbrooke, E., 2008. Effect of HIP'ping on deformation anisotropy in a single crystal Ni-based superalloy. Acta Materialia 56, 4349–4357.

Ebrahimi, F., Feroro, L., Siddiqui, S., Arakere, N.K., 2006. Effect of notch orientation on the evolution of plasticity in superalloy single crystals. Journal of Materials Science and Engineering A 426, 214–220.

Flouriot, S., Forest, S., Cailletaud, G., Koster, A., Remy, L., Burgardt, B., Gros, V., Mosset, S., Delautre, J., 2003. Strain localization at the crack tip in single crystal CT specimens under monotonous loading: 3D finite element analysis and application to nickel-based superalloys. International Journal of Fracture 124, 43–77.

Hashmin, Z., Shtrikman, S., 1962a. On some variational principle in anisotropic and nonhomogeneous elasticity. Journal of the Mechanics and Physics of Solids 10, 335–342.

Hashmin, Z., Shtrikman, S., 1962b. A variational approach to the theory of elastic behavior of polycrystals. Journal of the Mechanics and Physics of Solids 10, 343–352.

Kalluri, S., Abdul-Aziz, A., McGaw, M., 1991. Elastic response of [0 0 1]-oriented PWA 1480 single crystal – the influence of secondary orientation. SAE Transactions, vol. 100, SAE Paper 91-1111.

Kim, Y., Chao, Y.J., Zhu, X.K., 2003. Effect of specimen size and crack depth on 3D crack-front constraint for SENB specimens. International Journal of Solid and Structures 40, 6267–6284.

Kysar, J.W., Briant, C., 2002. Crack tip deformation fields in ductile single crystals. Acta Materialia 50 (9), 1367–1380.

Lekhnitskii, S.G., 1963. Theory of Elasticity of an Anisotropic Elastic Body. Holden-Day, San Francisco. pp. 1–40.

Magnan, S., 2002. Three-dimensional stress fields and slip systems in single crystal superalloy notched specimens. M.S. Thesis, Department of Mechanical & Aerospace Engineering, University of Florida, Gainesville, Florida.

Milligan, W.W., Antolovich, S.D., 1987. Yielding and deformation behaviour of the single crystal superalloy PWA 1480. Metallurgical Transactions 18A, 85.

Nalla, R.K., Campbell, J.P., Ritchie, R.O., 2002. International Journal of Fatigue 24, 1047.

Rice, J.R., 1987. Tensile crack tip fields in elastic-ideally plastic crystals. Mechanics of Materials 6, 317–335.

Rice, J.R., Saeedvafa, M., 1987. Crack tip singular fields in ductile crystals with taylor power-law hardening. Journal of the Mechanics and Physics of Solids 36, 189–214.

Saeedvafa, M., Rice, J.R., 1988. Crack tip singular fields in ductile crystals with taylor power-law hardening. II. Plane-strain. Journal of the Mechanics and Physics of Solids 37, 673–691.

Schulson, E.M., Xu, Y., 1997. Notch-tip deformation of Ni_3Al single crystals. In: MRS Proceedings, vol. 460, pp. 555–560.

Shield, T.W., 1996. Experimental study of the plastic strain fields near a notch tip in a copper single crystal during loading. Acta Materialia 44, 1547–1561.

Shield, T.W., Kim, K.S., 1994. Experimental measurement of the near tip strain field in an iron–silicon single crystal. Journal of the Mechanics and Physics of Solids 42, 845–873.

Siddiqui, S.A., 2006. Evolution of plasticity (slip) in notched single crystal superalloy specimens. Ph.D. Dissertation, Department of Mechanical & Aerospace Engineering, University of Florida, Gainesville, Florida.

Westbrooke, E.F., 2005, Effect of crystallographic orientation on plastic deformation of single crystal nickel-base superalloys, Ph.D. Dissertation, University of Florida.